



ELSEVIER

Available online at www.sciencedirect.com

SCIENCE @ DIRECT®

EPSL

Earth and Planetary Science Letters 212 (2003) 73–88

www.elsevier.com/locate/epsl

Coseismic displacements of the footwall of the Chelungpu fault caused by the 1999, Taiwan, Chi-Chi earthquake from InSAR and GPS data

Erwan Pathier^{a,*}, Bénédicte Fruneau^b, Benoît Deffontaines^c,
Jacques Angelier^a, Chung-Pai Chang^d, Shui-Beih Yu^e, Chyi-Tyi Lee^f

^a *Laboratoire de Tectonique, University of Paris 6, E1, T26, Case 129, 4 Place Jussieu, 75252 Paris Cedex, France*

^b *Institut Francilien des Géosciences, University of Marne-la-Vallée, 5 Boulevard Descartes, 75454 Marne-la-Vallée Cedex, France*

^c *Laboratoire de Géomorphologie et Environnement Littoral, EPHE, 15 Boulevard de la Mer, 35800 Dinard, France*

^d *Center for Space and Remote Sensing Research, National Central University, Chungli 320, Taiwan*

^e *Institute of Earth Sciences, Academia Sinica, P.O. Box 1-55, Nankang, Taipei, Taiwan*

^f *Institute of Applied Geology, Central University, Chungli, Taiwan*

Received 5 November 2002; received in revised form 16 April 2003; accepted 6 May 2003

Abstract

The differential SAR interferometry technique (interferometric synthetic aperture radar, InSAR) is applied on the Chelungpu fault surface rupture zone of the September 20, 1999, Taiwan, Chi-Chi earthquake using six ERS-2 images covering the period from February 1999 to January 2000. As compared with available geodetic data, InSAR measurements result in more extensive analysis because of high spatial sampling and centimetric accuracy. However, coseismic displacements can be evaluated only on the footwall of the fault. The analysis of interferograms shows the existence of a linear trend in phase difference mainly caused by orbital errors, which we removed from interferograms using GPS data. The corrected interferograms provide a precise map of the InSAR component of the coseismic displacement, showing a continuous decrease over the footwall from a maximum of 36.7 cm at the fault east of Taichung city to a value of about 5 cm at the coastline 30 km further west. The map analysis reveals that the Changhua fault (whose surface trace is located about 20 km west of the Chelungpu one) and the Tuntzuchio fault influence the displacement field. We interpret this in terms of minor reactivation of these faults triggered by the earthquake. A 1.7 cm uncertainty, estimated from the GPS data, is proposed to quantify the precision of the map. Beyond this single value, we highlight the interest of having several coseismic interferograms to evaluate the reliability of the map in a more comprehensive way. Comparisons with displacements inferred from models of slip distribution inverted without InSAR data highlight the advantage of carrying out a joint inversion including our results as new constraints.

© 2003 Elsevier Science B.V. All rights reserved.

Keywords: earthquakes; SAR; interferometry; GPS; coseismic processes; Taiwan

* Corresponding author. Tel.: +33-1-44-27-71-81; Fax: +33-1-44-27-50-85.

E-mail address: erwan.pathier@lgs.jussieu.fr (E. Pathier).

1. Introduction

On 21 September 1999, the $M_w = 7.6$ Chi-Chi earthquake occurred in central western Taiwan. This earthquake was related to an out-of-sequence reactivation of a major north–south-trending thrust of the Taiwanese Foothills, the Chelungpu fault [1,2] (Fig. 1). The deformation front of the fold-and-thrust belt of the Foothills is located 15–20 km west of the Chelungpu fault at the Changhua fault [3]. Rupture that developed over the Chelungpu fault plane reached the Earth's surface, causing a spectacular 90-km-long scarp between the hangingwall to the east and the footwall to the west [4]. Because of both the density and the quality of Taiwanese strong motion and Global Positioning System (GPS) networks, the Chi-Chi earthquake was among the best instrumentally recorded earthquakes. Several

analyses have been presented to quantify the earthquake surface displacements from GPS measurements [5,6], strong motion records [7], SPOT satellite optical images [8] and field measurements along the fault trace [9,10]. These results have been used to model the distribution of slip on the fault surface [11–14]. However, between the different resulting models, discrepancies remain in terms of geometry, slip distribution and predicted coseismic displacements.

Aiming to better constrain the coseismic displacement field of the Chi-Chi earthquake and consequently the models, this study uses data provided by interferometric synthetic aperture radar (InSAR). The InSAR technique is a complement to other geodetic methods because of its dense spatial sampling over a large surface, its precision and its high sensitivity to vertical displacement. In this paper, we first describe how we implement the

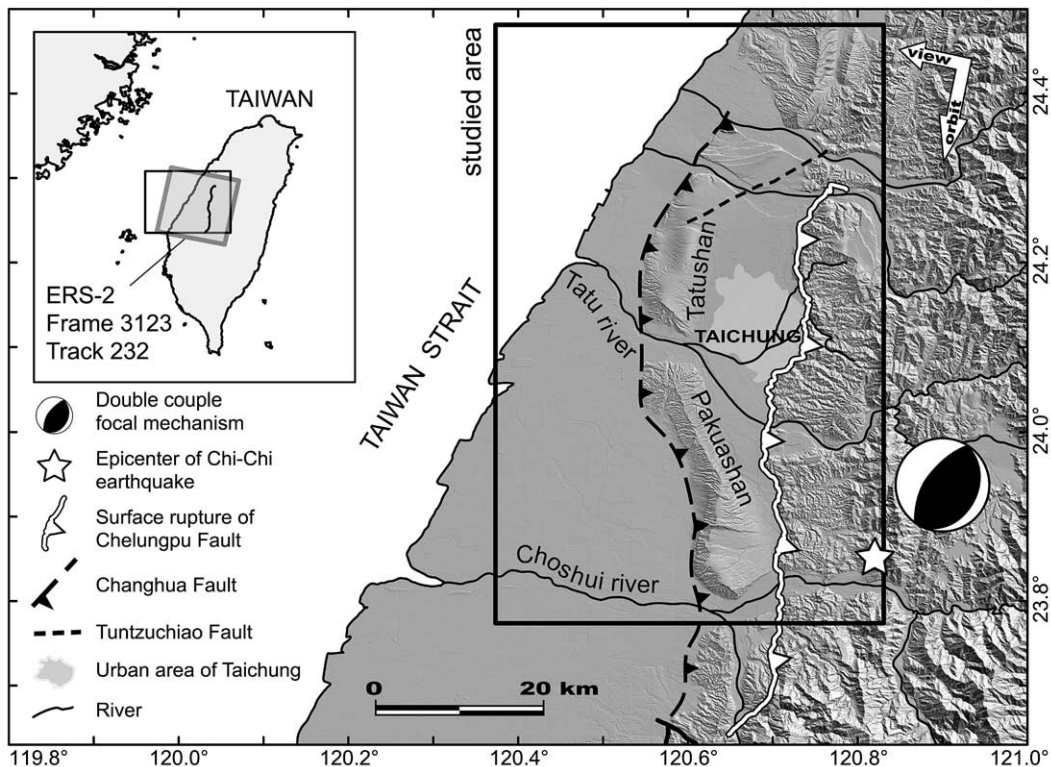


Fig. 1. Location of the footwall of the Chelungpu fault. Inset: The grey rectangle indicates the ERS SAR image frame used in this study; the black rectangle shows the location of the main figure. Main figure: in the background, shaded DEM of the epicentre area; the black rectangle shows the location of Figs. 3 and 4. The white arrows correspond to orbit track and viewing directions of the ERS satellite.

InSAR technique. Then, analysis of the resulting interferograms focuses on retrieving quantitative information about the permanent surface coseismic displacements. Corrections and processing are applied to the interferograms in order to obtain a map of InSAR coseismic displacements that permits geophysical analysis and interpretation, particularly on the behaviour of the Changhua and Tuntzuchio faults at the time of the Chi-Chi earthquake. Finally, we discuss the validity of the resulting map and we compare the results with two existing slip models of the Chelungpu fault.

2. InSAR: method and data

2.1. Method

For this study, we apply the InSAR technique in the two-pass approach using the DIAPASON software [15]. The method, also called differential InSAR, requires at least two SAR images of the same area acquired at two different times in similar conditions, topographic information on the studied area and satellite orbit information for both acquisitions. See Massonnet et al. [16] and Massonnet and Feigl [17] for details on requirements and limits of the method. As the main result, an image called an interferogram is produced, as a map of the phase difference $\Delta\Phi$ of both SAR images, so that for each pixel:

$$\Delta\Phi = \Delta\Phi_d + \Delta\Phi_a + \Delta\Phi_{te} + \Delta\Phi_{oe} + \Delta\Phi_{dc} + \Delta\Phi_n \quad (1)$$

where $\Delta\Phi_d$ is related to the displacement of the surface between the two acquisitions, $\Delta\Phi_a$ is related to the difference of atmospheric states, $\Delta\Phi_{te}$ is related to errors in the topographic model, $\Delta\Phi_{oe}$ depends on errors in orbital information, $\Delta\Phi_{dc}$ represents phase changes caused by geometric and temporal decorrelation, and $\Delta\Phi_n$ gathers phase changes due to thermal noise, SAR image processing errors and misregistration errors of both SAR images [18–20]. For a comprehensive review of these different terms see Hanssen [21].

For each pixel of an interferogram, $\Delta\Phi$ can record the displacement of the corresponding cell of resolution: $\Delta\Phi_d$ is proportional to the component of the full displacement vector along the radar line of sight. Hereafter, this component is called SRD (slant range displacement). We adopt the following convention: a positive SRD is from ground to satellite. An SRD that is $\lambda/2$ (λ being the radar wavelength) corresponds to a $\Delta\Phi_d$ equalling 2π radians.

Due to phase ambiguity, values of $\Delta\Phi$ are given modulo 2π . Phase ambiguity prevents access to absolute value, so that a $\Delta\Phi$ value from only one pixel is useless. However, such a value makes sense while measuring changes in $\Delta\Phi$ by comparison with other pixels. Measuring changes in $\Delta\Phi$ requires several conditions that limit interferogram analysis, especially low $\Delta\Phi_{dc}$ and $\Delta\Phi_n$ contributions and a not too high gradient of $\Delta\Phi$ [17]. $\Delta\Phi_{dc}$ and $\Delta\Phi_n$ terms induce changes in $\Delta\Phi$ that are not coherent from one pixel to another. Once coherent changes in $\Delta\Phi$ on the interferogram have been identified, the analysis of interferograms consists in estimating the part of the different contributions of $\Delta\Phi$. For our purpose, which is to extract SRD information from interferograms, the main goal is to estimate $\Delta\Phi_d$ values.

2.2. The data

We selected six SAR images in order to obtain several coseismic interferograms that we can compare. The SAR image selections have been based on two major criteria: making their baselines (distance between two orbit trajectories) as short as possible, which results in smaller $\Delta\Phi_{te}$ and $\Delta\Phi_{dc}$ contributions, and having the shortest time interval between acquisitions in order to reduce the temporal decorrelation effects.

Regarding the choice of the SAR sensor, no JERS images being available since 1998, we retained ERS (European remote sensing satellite) data because they offered more possibilities than Radarsat to obtain several coseismic couples meeting the requirements. In addition, a previous study [22] had demonstrated the feasibility of InSAR measurements with ERS data in the Foot-hills of southwestern Taiwan. Finally, we used

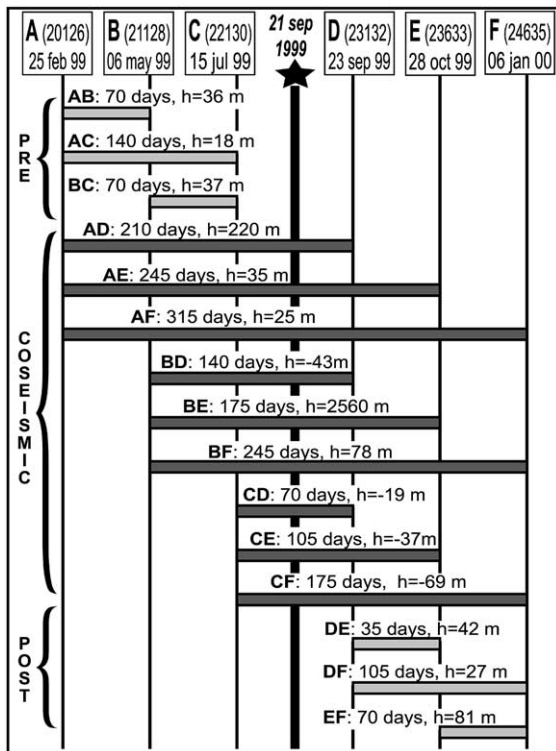


Fig. 2. ERS data list. List of the 15 interferograms processed from the six ERS2 SAR images. Orbit number and date of acquisition of each image (A,B,C,...) are given. Each grey bar corresponds to an interferogram with its name used in this paper, its time span and its height of ambiguity (h , in metres).

only images from the SAR sensor of ERS-2 operating at 5.3 GHz ($\lambda=5.6$ cm), as no ERS-1 images covered the earthquake period. We chose images in descending orbit, because the shortest time interval (about 3 years) available in ascending mode was too long.

In order to capture the coseismic SRD, we selected three images acquired before and three images after the earthquake (Fig. 2). All of these images cover the same zone (Track 232, frame 3129, see location in Fig. 1) corresponding to the fault zone. The other data we used are a 40 m \times 40 m grid spacing DEM (digital elevation model) with a vertical accuracy of about 5 m, and precise orbits of ERS-2 determined by the Delft Institute for Earth-Oriented Space Research [23].

3. Interferogram analysis

3.1. Detection of coseismic displacements and perturbations

Among the 15 resulting interferograms, three span a preseismic period, nine a coseismic one,

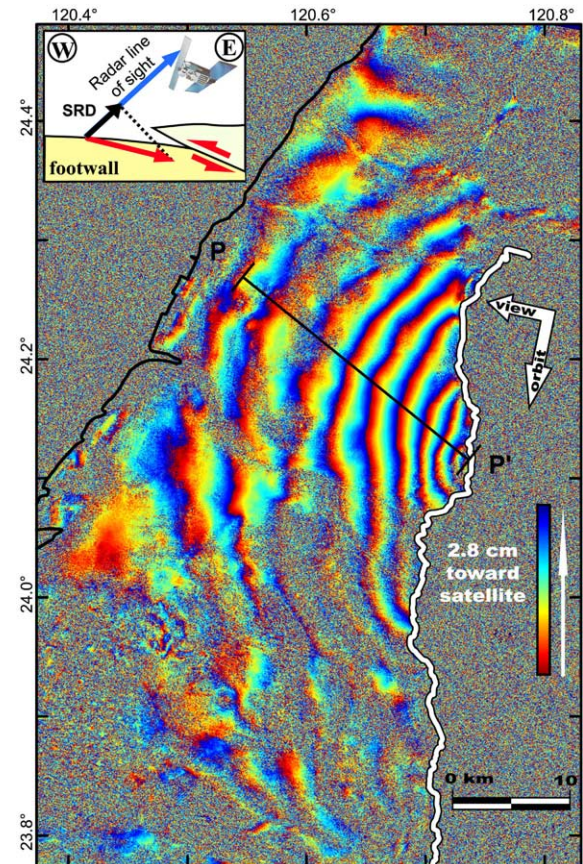


Fig. 3. Coseismic interferogram of the Chi-Chi earthquake. Filtered interferogram AD (25 Feb. 99–23 Sept. 99) showing coseismic displacement. To first order, each cycle of colour (a fringe) from blue to red corresponds to 2.8 cm of relative displacement toward the satellite. White thick line, Chelungpu fault trace; black line, coastline; black segment, location of profile PP' (see Fig. 4). Inset: Geometry of acquisition. The red vector represents the coseismic displacement; the black vector corresponds to the SRD measured by InSAR (projection of the red vector on the radar line of sight). The three components of the unit vector from ground to satellite, at the centre of the studied area, expressed in local terrestrial reference are: up=0.924, east=0.375, north=-0.079. These components vary gently over the interferogram, the incidence angle ranging from 20.5 to 24.9° on the studied area.

and three a postseismic one (Fig. 2). The coherence of these different interferograms is principally a function of the baseline and of the time interval: the smaller these parameters are, the better the coherence is. In all coseismic interferograms, there is coherent information only in the footwall area (Fig. 3). Even in pre- or postseismic interferograms, most of the hangingwall domain lacks coherence (Fig. 4b). The footwall is largely urbanised, which favours numerous stable scatterers having a low temporal decorrelation, whereas the hangingwall is essentially covered by dense vegetation, causing rapid temporal phase decorre-

lation. Two other factors accentuate this contrast: (1) as shown by GPS [6], the displacement gradients close to the fault are much larger in the hangingwall than in the footwall and could exceed the upper limit of the phase gradient discernible by ERS InSAR (about 10^{-3} [21]); (2) the deformation and earthquake destruction in the hangingwall contribute to phase decorrelation in the affected cells of resolution.

In the footwall, coseismic interferograms show a similar pattern formed by a dozen fringes as illustrated in Fig. 3. As these fringes are present in all coseismic interferograms and because they

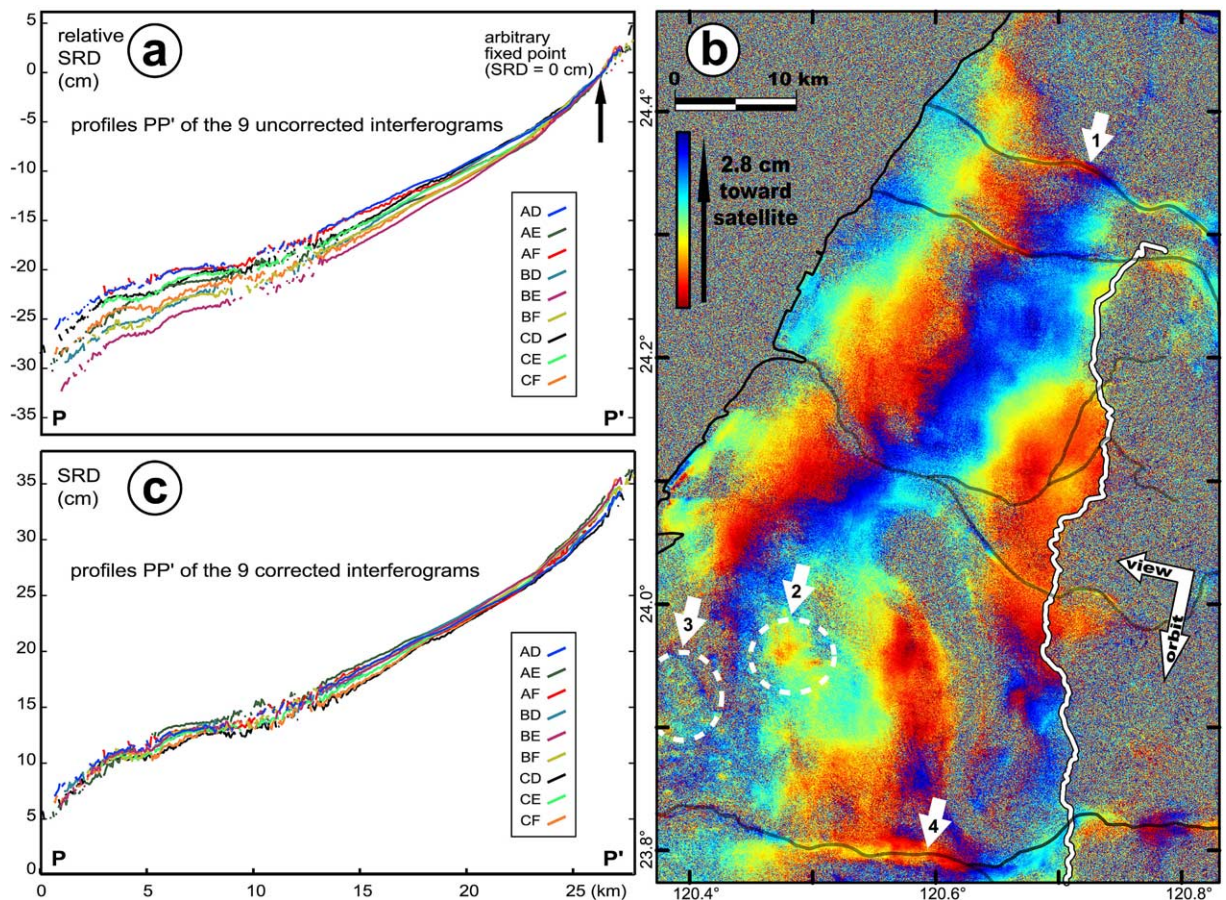


Fig. 4. Perturbations affecting the InSAR measure of the coseismic displacements. (a) Profile PP' (location in Fig. 3) of unwrapped and uncorrected coseismic interferograms, showing large-scale perturbation. (b) Pre-seismic filtered interferogram AB showing large fringes mainly related to orbital errors and locally disturbed by medium-scale perturbations. White arrows show location of non-coseismic displacement: 1 and 4, perturbations at river beds; 2 and 3, subsiding areas located west of Pakuashan (see Section 3.2). (c) Profile PP' of unwrapped coseismic interferograms after linear trend correction by GPS.

are consistently correlated with the fault trace, we interpret the major part of these changes in $\Delta\Phi$ as being $\Delta\Phi_d$ changes related to coseismic displacement of the ground surface. Thus, in first approximation, the fringes can be read as contour lines (with a spacing of $\lambda/2$, that is 2.8 cm) of a contour map of coseismic SRD. Under this hypothesis, there is an increase in SRD towards the fault trace relative to a point at the coastline chosen as reference. The highest SRD values are close to the fault, in the fault trace concavity east of the city of Taichung. Taking into account the radar line of sight direction (Fig. 3), interferograms give constraints on three-dimensional coseismic displacements. Additional sources of information on the coseismic displacements, such as GPS data, locally help to remove ambiguity on full vector displacement and improve the interpretation. Note that in the particular case of our InSAR observation of the Chi-Chi earthquake the coseismic interferograms indicate positive SRD although the GPS indicates a downward displacement of the footwall. As illustrated in Fig. 3, this situation results from a greater horizontal displacement moving the ground closer to the satellite than the vertical displacement moving the ground away from the satellite.

Fig. 4a, which illustrates the different SRDs inferred from the nine coseismic interferograms assuming $\Delta\Phi = \Delta\Phi_d$ on coherent pixels, shows that this hypothesis needs to be refined. The discrepancies in SRD indicate that, although the main part of the changes in $\Delta\Phi$ in coseismic interferograms can be interpreted as coseismic displacements, the resulting fringes are also more or less influenced by other factors, as mentioned in Eq. 1, as well as by non-coseismic displacements (coseismic interferograms cover a time period larger than the coseismic event period). Hereafter we call perturbations the changes in $\Delta\Phi$ that are not caused by coseismic displacements.

In the absence of perturbation, coseismic interferograms should be identical and pre- and post-seismic ones should not show any coherent change in $\Delta\Phi$. In fact, we observed perturbations in interferograms that can be decomposed into three main types. The first kind of perturbations affects the whole interferogram (hereafter large-

scale perturbation) and consists of a relatively constant gradient of $\Delta\Phi$ for a given interferogram. In pre- and postseismic interferograms (AB, BC, DE and EF), where they are best expressed, such large-scale perturbations are represented by large and roughly parallel fringes (Fig. 4b). In coseismic interferograms, they are superimposed on the coseismic signal, inducing large trend variations (Fig. 4a). The second kind of perturbation consists of kilometre- to hectometre-scale smooth variations of $\Delta\Phi$ (hereafter medium-scale perturbations) that give an irregular aspect to the interferogram and disturb the large-scale fringe in pre- and postseismic interferograms (Fig. 4a,b). The third kind of perturbation (hereafter small-scale perturbation) corresponds to rapid change from one pixel to the nearest pixel, well expressed in lower-coherence area and resulting in a ‘noisy’ aspect in the interferograms.

3.2. Origin of perturbations

The small-scale perturbations are mainly related to $\Delta\Phi_{dc}$ and $\Delta\Phi_n$ terms. Considering large-scale perturbations, their fringe pattern (Fig. 4b) is typical of residual orbital fringes related to errors in positioning of orbit trajectories. We cannot exclude, however, a large-scale atmospheric effect, or a combination of both of these origins. The variability with time in direction and magnitude of these perturbations indicates that large-scale displacements (tectonic or not) cannot contribute much to these gradients. This observation also discards a perturbation due to large-scale DEM errors ($\Delta\Phi_e$), because it is expected always to have the same direction whatever the interferogram considered and to have a magnitude proportional to the baseline.

If we interpret these phase gradients as only caused by errors on the baseline values, the highest gradient will correspond to an error of about 1 m. Note that such errors are larger than those expected with a 95% likelihood for DEOS precise orbit that we used [21]. We also compute pre-seismic interferograms with other orbital data: the DLR precise orbits [24]. The resulting interferograms present a slightly higher $\Delta\Phi$ gradient and it is noteworthy that the orientation of fringes re-

sembles those obtained with DEOS orbits. This observation argues for an orbital error origin, because if these fringes were mainly caused by large-scale atmospheric perturbation in interferograms processed with DEOS orbits, parallelism between such fringes and those introduced by the DLR orbit error would be unlikely. On the other hand, such parallelism can result from similar calculation methods for the two kinds of orbits. This leads us to assume that the major part of the large-scale phase gradient is due to orbital errors (these errors also cause perturbations correlated with the relief; however, in our case, their low values make these effects negligible).

Regarding the medium-scale perturbations in pre- and postseismic interferograms, we exclude a significant influence of $\Delta\Phi_{te}$ because medium-scale perturbations are not correlated with the baseline. Direct observations of interferograms show that most of the perturbations are changing in space from one interferogram to another. Thus, we suppose an atmospheric main origin for most of them. These perturbations are not visibly correlated with the relief on the footwall. The topography of the footwall ranges from 0 m near the coast to 450 m at Pakuashan, and 60% of coherent points have elevation less than 100 m, which is moderate compared to relief where correlation between atmospheric effect and topography have been found in other studies [25]. Note that we do not propose to evaluate the correlation between $\Delta\Phi$ and the topography using the GPS data as control because of the number of GPS points available and their altitude distribution: 18 of the 28 stations that we used are below 100 m elevation and the highest station (TECS) has an elevation of only 245 m. We finally consider in first approximation that most of the medium-scale perturbations are randomly variable in magnitude and location from one interferogram to another. We extrapolate this assumption, made on pre- and postseismic interferograms, to coseismic interferograms, where perturbations and coseismic effects are mixed, which makes such an analysis difficult.

However, to a lesser extent, other kinds of medium-scale perturbations are constant in location (Fig. 4b). Slight changes in $\Delta\Phi$ that are exactly

located at river beds could be linked to the local variation of the water vapour content in the atmosphere due to the presence of the rivers. These changes in $\Delta\Phi$ could also be interpreted as non-coseismic subsiding displacements. We also incriminate non-coseismic displacement (subsidence) to explain systematic changes in all of the pre- and postseismic interferograms at two locations west of the Pakuashan hills (Fig. 4b). Other non-coseismic displacements can affect the interferograms. Such displacements involve pre-seismic secular motion (recorded by the GPS), displacements caused by postseismic slip on the fault or by aftershocks. Postseismic subsidence or rebound phenomena could be notably caused by the widespread coseismic change in pore water pressure recorded by the network of hydrologic monitoring wells [26]. However, as they cannot be detected by direct observation of the interferograms, the magnitudes of such displacements are small compared to the perturbations caused by the atmospheric effects.

4. Interferogram correction from GPS data

4.1. The GPS data

As we have no sufficient information about orbital error or atmospheric effect, we cannot determine how far the coseismic interferograms are affected by the perturbations in the absence of an a priori knowledge of the coseismic displacements. External information is needed in order to achieve the coseismic displacement estimation.

GPS data can give such information about the coseismic displacements. This information is punctual and gives an absolute displacement, whereas InSAR covers large areas and indicates relative displacement. The comparison with GPS data requires unambiguous phase information, which we obtain by unwrapping all the interferograms using a semi-automatic method based on ‘residu-branch-cut’ algorithm [27] with possible manual intervention to connect isolated unwrapped areas when the automatic process fails. The number of pixels unwrapped in an interferogram (see Table 2) depends of its quality. To fa-

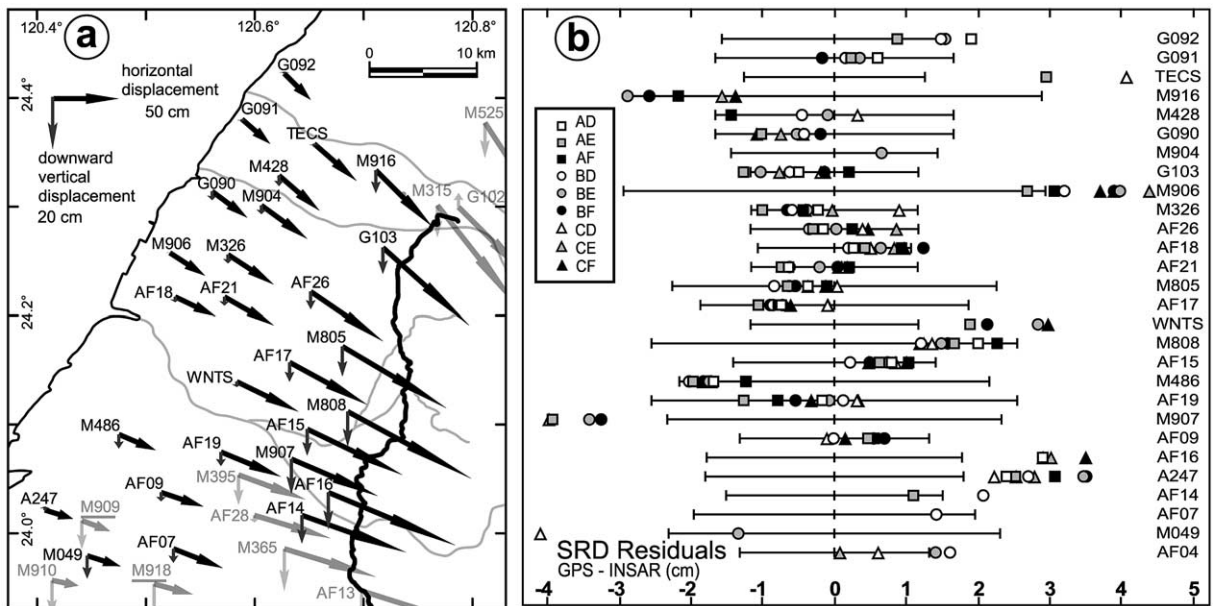


Fig. 5. GPS data and comparison with corrected InSAR data. (a) Map of the coseismic displacements at GPS stations from Yu et al. [6]; stations in faint grey are not used in this study, the two underlined stations (southwest corner) have been discarded from the selection (see text). (b) Residuals of the interferogram corrections: the black lines are the GPS error bars at each station sorted by latitude. The squares, circles and triangles indicate the difference (in cm) between the coseismic displacements along the radar line of sight (SRD) inferred from GPS data at each station and the SRD from each corrected interferogram.

cilitate unwrapping, we apply a filter that smooths the small-scale perturbations [28]. The spatial distribution of the available GPS stations in the footwall from Yu et al. [6] (Fig. 5a) allows us to constrain the large-scale perturbations, but is too sparse to constrain the medium-scale perturbations. Among the 59 stations in the footwall, 54 are in the InSAR-studied area. We used only 28 of these 54 stations because the other 26 are located outside all unwrapped areas of our coseismic interferograms. In addition, two GPS stations (M918 and M909, see location in Fig. 5a) are discarded because they reveal large differences with respect to the corrected interferograms (about -12 and -18 cm, respectively) and seem poorly representative of the regional displacement with respect to the neighbouring stations. The uncertainties given for these two stations resemble those of other stations, so that local site effects that would have affected these two stations may account for the discrepancy. Amongst the 28 selected stations, 12 stations always have their cor-

responding pixel unwrapped in all of the interferograms (Table 1).

Yu et al. [6] corrected the data for preseismic secular motions by fitting the velocity of 24 stations (surveyed from 1992 to 1999), by a first-order trend surface. They also made postseismic corrections, but at the stations that we selected they indicate that there are no postseismic displacements. As our interferograms are not exactly coseismic, we adapt the preseismic corrections made on GPS data for each interferogram according to the date of its preseismic image, assuming a preseismic secular motion constant with time (Table 1). According to this method, the amount of preseismic SRD is maximal in the interferograms using image A. In this case, taking into account the 28 selected stations, the standard deviation of preseismic SRD is 0.18 cm and the average value is 0.1 cm. The extreme values are at stations TECS (-0.5 cm) and M049 (0.5 cm). The perturbations caused by preseismic displacement are minor relative to those observed that are mainly due

Table 1
GPS data used for interferogram corrections

Station	Latitude (°)	Longitude (°)	East ^a	North ^a	Up ^a	East ^b	North ^b	Up ^b	Cos. ^c	AX ^d	BX ^d	CX ^d	# ^e
A247	120.408	24.020	21.3	−6.2	1.7	0.397	−0.083	0.914	10.5	10.4	10.4	10.5	9
AF04	120.534	23.871	32.3	−6.7	−5.2	0.379	−0.080	0.922	8.0	7.7	7.8	7.9	4
AF07	120.525	23.985	37.9	−14.8	−5.3	0.383	−0.081	0.920	10.8	10.5	10.6	10.7	1
AF09	120.514	24.037	33.2	−10.7	−3.3	0.385	−0.081	0.919	10.6	10.3	10.4	10.5	7
AF14	120.643	24.015	79.2	−28.4	−10.4	0.370	−0.078	0.926	21.9	21.8	21.8	21.9	2
AF15	120.648	24.094	72.6	−35.3	−10.1	0.372	−0.079	0.925	20.4	20.3	20.3	20.4	9
AF16	120.668	24.036	96.2	−39.9	−14.3	0.368	−0.078	0.927	25.3	25.2	25.2	25.2	4
AF17	120.632	24.156	59.1	−32.1	−7.4	0.375	−0.079	0.924	17.9	17.8	17.8	17.8	9
AF18	120.527	24.216	31	−15.8	−2.4	0.388	−0.082	0.918	11.1	11	11	11.1	9
AF19	120.569	24.073	45.7	−18.8	−4.9	0.380	−0.080	0.921	14.4	14.2	14.2	14.3	9
AF21	120.572	24.216	37.9	−22.2	−3.6	0.383	−0.081	0.920	13.0	12.9	13	13	9
AF26	120.651	24.221	55.8	−38.3	−6.7	0.375	−0.079	0.924	17.7	17.7	17.7	17.7	9
G090	120.562	24.312	26	−20.2	−3.3	0.387	−0.081	0.919	8.7	8.6	8.6	8.6	7
G091	120.589	24.379	21.2	−19.1	−0.8	0.386	−0.081	0.919	9.0	8.9	8.9	9	5
G092	120.628	24.421	19.4	−19.8	0.8	0.382	−0.081	0.921	9.7	9.7	9.7	9.7	4
G103	120.718	24.260	66.3	−59.2	−10	0.368	−0.078	0.927	19.8	19.8	19.8	19.8	9
M049	120.446	23.979	26	−8.1	−8.6	0.391	−0.082	0.917	3.0	2.5	2.7	2.8	2
M326	120.575	24.254	35.3	−22.6	−3.4	0.384	−0.081	0.920	12.3	12.2	12.2	12.2	9
M428	120.622	24.327	30.9	−27.1	−4.2	0.381	−0.080	0.921	10.1	10.2	10.2	10.1	4
M486	120.475	24.090	29	−12.3	−5.5	0.391	−0.082	0.917	7.3	6.9	7.1	7.2	9
M805	120.681	24.171	79.8	−47.4	−11.5	0.370	−0.078	0.926	22.6	22.5	22.6	22.6	9
M808	120.686	24.111	93.7	−51.7	−13.3	0.368	−0.078	0.927	26.2	26.1	26.1	26.2	9
M904	120.607	24.299	33.8	−25.5	−2.9	0.382	−0.080	0.921	12.3	12.4	12.4	12.3	1
M906	120.522	24.256	27.9	−18.1	0.1	0.390	−0.082	0.917	12.5	12.2	12.3	12.4	8
M907	120.633	24.068	67	−29.5	−13.9	0.373	−0.079	0.925	14.4	14.3	14.4	14.4	4
M916	120.712	24.332	42.9	−43	−8.6	0.371	−0.078	0.925	11.3	11.3	11.3	11.3	5
TECS	120.655	24.356	31.7	−28.2	−0.4	0.378	−0.080	0.922	13.9	14.4	14.2	14	2
WNTS	120.584	24.138	46.8	−22.3	−2.3	0.380	−0.080	0.921	17.5	17.6	17.6	17.5	4

^a Components (cm) of the coseismic displacement from [6] corrected for preseismic secular motion.

^b Unit vector from ground to satellite at the station.

^c Coseismic displacement along the SRD (cm) at the station.

^d SRD (cm) integrating the coseismic displacement and the preseismic secular motion for an interferogram XX (with $X=A, B$ or C).

^e Number of coseismic interferograms where a given station corresponds to a coherent pixel.

to atmospheric effect. We do not correct the interferograms from the preseismic SRD, because of the difficulty to estimate a velocity trend surface that is controlled only by four GPS stations in our interferograms and because of high uncertainties of the preseismic SRD reconstructed from GPS data relative to their magnitudes.

4.2. Model and method

For each interferogram, we model the large-scale perturbation by a phase ramp characterised by two constant gradients along east–west and north–south direction, which implies that these

large-scale perturbations for an interferogram correspond to equally spaced parallel fringes. Our approach is similar to that of Murakami et al. [29]: we compute the difference between each unwrapped interferogram and the GPS measurements to perform a least-squares adjustment. In this least-squares adjustment the model is expressed by:

$$V_i = G_{E-W} X_i + G_{N-S} Y_i + C \quad (2)$$

where V_i is the difference between the interferogram and GPS at the i th GPS station, X_i and Y_i are the coordinates of the corresponding pixel of

Table 2
Coseismic interferogram information

Name	Unwrapped ^a (%)	E–W ^b (10 ^{−5})	N–S ^b (10 ^{−5})	GPS stations ^c	GPS rms diff. ^d (cm)	SRD map rms diff. ^e (cm)
AD	0.73	−0.02	−0.08	15	1.35	0.31
AE	0.72	−0.10	−0.06	21	1.67	0.62
AF	0.56	0.00	−0.02	16	1.5	0.59
BD	0.95	−0.19	−0.35	21	1.34	0.35
BE	1	−0.32	−0.33	24	1.72	0.31
BF	0.78	−0.21	−0.27	19	1.76	0.33
CD	0.69	−0.11	−0.09	21	2.02	0.58
CE	0.63	−0.21	−0.05	17	1.67	0.57
CF	0.7	−0.10	−0.02	18	1.69	0.41

^a Proportion of unwrapped pixels with respect to interferogram BE (626817 unwrapped pixels).

^b E–W and N–S gradients of large-scale perturbation (10^{−5} or cm/km).

^c Number of GPS stations used to calculate the gradients.

^d Rms difference between the displacements along the radar line of sight (SRD) at GPS stations and the SRD given by a corrected coseismic interferogram.

^e Rms differences between the SRD map (average of interferograms AD, BE et CF) and the SRD of a given coseismic interferogram.

the i th GPS station, G_{E-W} and G_{N-S} represent the two gradients of phase ramp and C is the constant between the interferogram and GPS data. To compute the V_i value, we transform the three components of the GPS displacement vector into an SRD value, taking into account the local unit vector from ground to satellite given in Table 1. The adjusted phase ramp is then subtracted from the interferogram, resulting in a corrected interferogram. Relative changes in $\Delta\Phi$ in interferogram are measured only to within an additive constant, which is estimated by the parameter C in Eq. 2. Then, a constant correction is also applied changing from relative to absolute unwrapped interferograms. This method assumes that errors on GPS data do not introduce a systematic bias.

Theoretically, the GPS data could be used for more complex modelling of the $\Delta\Phi$ perturbation (e.g. by polynomial or spline methods). We justify our model for two main reasons. First, we assume that large-scale perturbations are mainly caused by orbital errors. In such a case, this model, which has already been used successfully [30], is acceptable if there are few residual orbital fringes and if the study area is only a portion of an ERS scene. In this study, these conditions are fulfilled, as illustrated by the pre- and postseismic interferograms (Fig. 4b). Second, considering the num-

ber of available GPS data, this simple model limits the possible influences of GPS data errors on interferogram corrections. The results of the adjustment are listed in Table 2.

5. InSAR coseismic displacement map

Comparison between Fig. 4a,c illustrates the results of the corrections that remove the large-scale perturbations. The differences between coseismic SRD calculated from GPS measurements and SRD obtained from corrected interferograms at each GPS station are given in Fig. 5b. It shows that differences are less than ± 4.5 cm and mainly lie within the error bars of the GPS data. The root mean square (rms) differences for each interferogram range from 1.35 to 2.02 cm (Table 2). Taking into account the nine coseismic interferograms the rms difference is 1.66 cm. The absence of significant large-scale residual perturbations in the corrected interferogram supports the phase ramp model that we adopted. In the corrected interferograms, medium- and small-scale perturbations remain, which are principally related to the atmospheric effect and cannot be modelled with GPS data. The dispersion of the corrected $\Delta\Phi$ values is expressed in Fig. 6a: it shows for each pixel the standard deviation of the nine $\Delta\Phi$

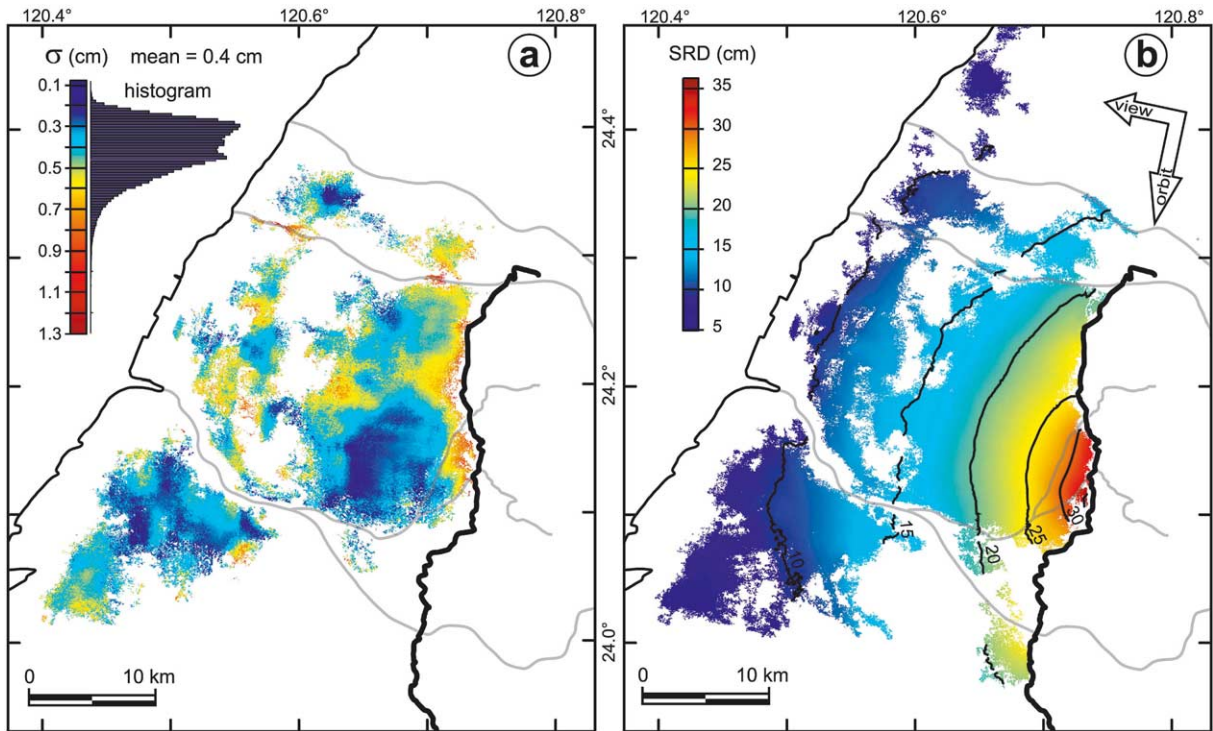


Fig. 6. Standard deviation of corrected coseismic interferograms and map of coseismic SRD. (a) Standard deviation σ (cm) of the corrected coseismic interferograms. Black thick line, Chelungpu fault; light grey line, rivers. σ is calculated only where the nine coseismic interferograms have been unwrapped. (b) Map of coseismic SRD that is the mean of the corrected interferograms AD, BE and CF. Thin black lines are iso-contours of SRD in cm. The white arrows correspond to orbit track and viewing directions of the satellite. The map shows a continuous seaward decrease in SRD, with a maximum at the concavity of the Chelungpu fault trace near the city of Taichung. The global trend is a seaward decrease in SRD gradient (spaces between iso-contours are wider).

values available for this pixel (only the pixels that have been unwrapped in all of the nine coseismic interferograms are thus considered). These values are quite constant over the available pixels, except for river anomalies where standard deviations reach 1.38 cm. The mean standard deviation is 0.4 cm.

To reconstruct the coseismic SRD map (Fig. 6b), we average the coseismic interferograms, expecting that this averaging should reduce the main unmodelled perturbations. This assumes a random distribution of the perturbations, as one can reasonably expect considering the observed atmospheric perturbations. Rather than using the nine available coseismic interferograms, we consider a combination of independent interfero-

grams. The six SAR images allow us to choose amongst three possible combinations of three independent interferograms. The most coherent combination is obtained with AD, BE and CF interferograms. This method yields more reliable points than that using the nine interferograms. The rms differences between each coseismic interferograms and the coseismic SRD map range between 0.3 and 0.6 cm (Table 2), showing good consistency between the coseismic interferograms. We propose to use the rms difference between GPS and all the coseismic interferograms, which is 1.7 cm, as an uncertainty for the map (see discussion in Section 6.1).

The map of the coseismic SRD shows displacements ranging from 36.7 cm (in the westward-

concave bend of the Chelungpu fault near Tai-chung) to 4.9 cm near the coast of the Taiwan Strait. There is a seaward continuous decrease in SRD (Figs. 4c and 6b). Considering the gradient of SRD, the global trend is a decrease of the gradient from the fault trace to the coastline (Fig. 7). Looking in detail at the displacement gradient, we locally observe a quasi-systematic re-increase of the gradient from east to west, which contrasts with the global decrease towards the west. This anomaly (arrows 1 in Fig. 7) follows a line that exactly corresponds to the Changhua fault trace. This observation is significant with respect to the uncertainties of the map. One may question the origin of this anomaly, as the profiles P_1P' , P_2P' and P_4P' in Fig. 7 show that the gradient anomaly is (as the fault) correlated with a topographic feature. However, we observed a similar change in gradient in profile

P_3P' , which crosses the Changhua fault in a flat plain area: an artefact that would be correlated with the relief is thus ruled out. We consequently interpret this anomaly as related to the Changhua fault, whose surface trace is located 10–20 km further west of the Chelungpu fault. To explain this anomaly, we propose that a minor reactivation of the Changhua fault zone may have occurred in response to the Chi-Chi earthquake, a phenomenon similar to that reported by Genrich et al. [31] in California (see also [32,44], who make reference to other triggered slip). This triggered reactivation does not necessarily reveal fault slip reaching the surface; it may reflect surface flexuring in a relatively narrow zone, related to deeper reactivation of the Changhua thrust ramp. In any case, such a displacement along the Changhua fault would account for the change in coseismic displacement field that induced the SRD gradient

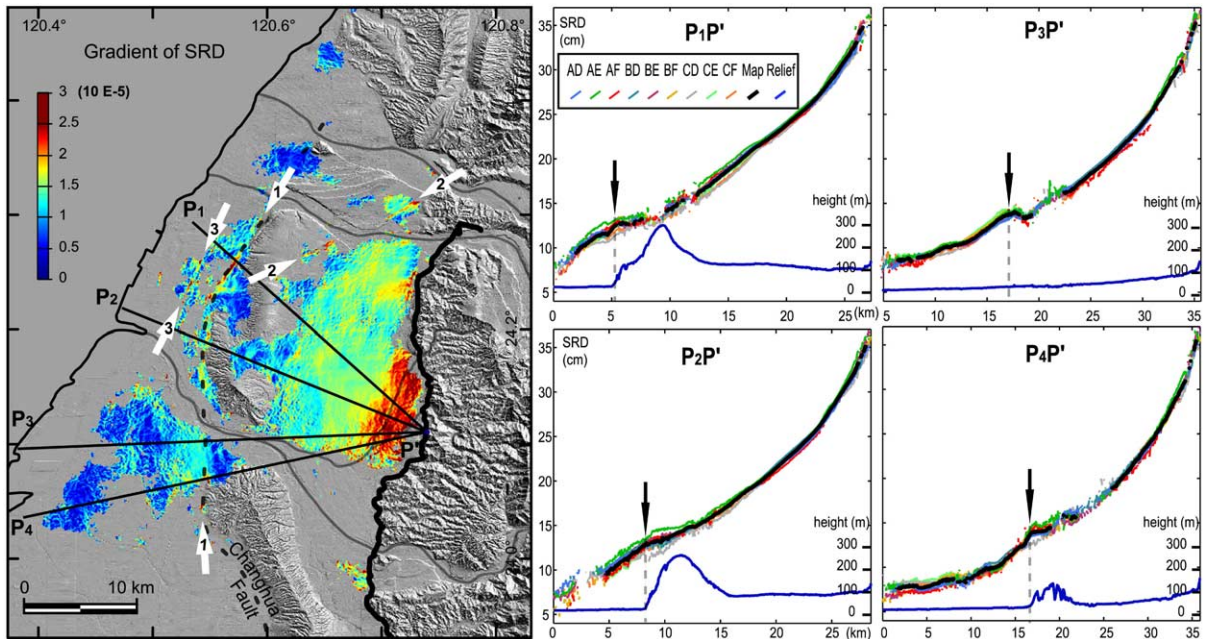


Fig. 7. Effect of the Changhua fault on the coseismic displacement field. (a) Map of gradient of coseismic SRD (with low-pass filter). It shows a global trend: a decrease (from red to dark blue) from east to west. The Changhua fault (dark grey dashed line) exactly fits an anomaly in this trend indicated by the white arrows 1. This anomaly, characterised by a re-increase in SRD from east to west, separates a blue-green area to the east from a red-yellow-green area to the west, contrasting with the global trend. White arrows 2 indicate an anomaly that corresponds to the Tuntzuchio fault (compare with Fig. 1). White arrows 3 indicate another, similar anomaly that could correspond to an unknown fault. (b–e) Four profiles (location in panel a) of the corrected coseismic interferograms, of the SRD map (black line) and of the relief (thin blue line) illustrating the anomaly 1. The black arrows show the location of the re-increase in SRD gradient. The profile P_3P' , which crosses a flat area, also shows the anomaly excluding an artefact linked to the relief.

anomaly that we observed. Similar observations and analyses can be made regarding two other anomalies indicated by arrows 2 and 3 in Fig. 7. Anomaly 2 exactly fits the surface rupture of the Tuntzuchio fault caused by the major 1935 earthquake [33] (see location in Fig. 1). Anomaly 3, west of the Changhua fault, does not correspond to an identified fault; however, following the two other correlations it is possible that this anomaly also corresponds to a fault.

6. Discussion and conclusion

6.1. Reliability of results

To quantify the reliability of our coseismic SRD map, we have proposed to attribute an uncertainty value of 1.7 cm to the map, using the rms difference between the SRD calculated from GPS data and the SRD of the nine coseismic interferograms. This value is greater than the usual estimation of the uncertainty corresponding to the rms difference between GPS data and the SRD map, which is 1.2 cm in our study. These two estimates are affected by the GPS errors, which can be more than 3 cm in SRD, causing an overestimate of the map uncertainty. The mean standard deviation of the coseismic interferograms (Fig. 6a), which is also an indicator of the uncertainty of the SRD map, is 0.4 cm. Then, the uncertainty evaluated from GPS data may be overestimated; however, the standard deviation of coseismic interferograms depends on nine measures that are not completely independent and does not take into account possible systematic errors in coseismic interferograms. Moreover, GPS data are not really independent of the SRD map, because they are used to evaluate the phase ramp gradients and the constants of the interferograms (parameters G_{E-W} , G_{N-S} and C , respectively, in Eq. 2). Thus, GPS data could introduce systematic errors in the SRD map that are not taken into account by the previous methods. Finally, as a precaution, we retained the 1.7 cm uncertainty given by the first method that is likely an upper bound throughout the map.

If such a single value is statistically representa-

tive of the uncertainty of the coseismic SRD map, it does not express the spatial variation of the uncertainty across the map. The map of standard deviation (Fig. 6a) is more informative to assess these variations than to consider the changes, from one GPS station to another, of the difference between GPS data and the SRD map. Fig. 6a shows that the highest values of the standard deviation map are distributed over areas of several kilometres, for example at a river bed north of Taichung or close to the fault. Regarding the different sources of errors of the coseismic SRD map, atmospheric effects and non-coseismic displacements are the main errors that can explain this spatial distribution. Changes in atmospheric state are not evenly distributed and can result in areas where variability between interferograms is high. Non-coseismic displacements can also produce a similar pattern in the spatial distribution. To distinguish between atmospheric effects and non-coseismic displacements, we need to analyse the temporal evolution between interferograms: atmospheric perturbations are expected to have no continuous evolution with time. For instance, regarding the variability close to the fault trace, both origins can be suspected. The area is located along a height change in the topography that can favour atmospheric variation. Regarding non-coseismic displacements, significant postseismic displacements are observed in the hangingwall by GPS [34,35], and also by InSAR (small hangingwall areas in postseismic interferograms show fringes that are consistent with deformation revealed by the GPS analysis). These displacements are related to a postseismic slip on the fault [34]. Thus, postseismic displacements on the footwall are possible near the fault trace. Yu et al. [6] did not apply any postseismic correction in the footwall. However, the GPS network coverage is low close to fault. The analysis of the temporal evolution between interferograms shows that the SRDs do not follow the logic of postseismic displacements and that their variations have rather an atmospheric origin. If the postseismic displacements suspected in this part of the footwall exist, they are too small relative to the atmospheric effects to be detected by our InSAR analysis. The SRD temporal analyses made at the

gradient anomalies (see Fig. 7) lead to similar conclusions.

This discussion illustrates the limit of an estimate of the uncertainty only based on GPS data and shows the importance of having several coseismic interferograms to better determine the spatial distribution of the uncertainties on the coseismic SRD map. Moreover, several coseismic interferograms allow analysis of the temporal evolution of the perturbations and, for instance, the revealing of non-coseismic displacements that are disregarded by the GPS network. This is particularly important as the shortest coseismic interferogram is not necessarily the best in quality.

6.2. Comparison with modelling of the distribution of slip on the fault plane

Complementing information obtained from seismicity, geodetic data have notably been used to constrain the distribution of slip on the fault surface of the Chi-Chi earthquake. Discrepancies exist between the different published slip distribution models of the fault owing to different geometries of the fault, different inversion methods and data sets. Regarding the data, most of the models are determined by the inversion of both GPS and strong motion data [7,13,14,36]. Ma et al. [11] also include teleseismic data, whereas Johnson et al. [12] use only GPS data and Chi et al. [37] only strong motion data. Dominguez et al. [8] combine GPS data with horizontal coseismic displacement inferred from correlation of SPOT satellite images.

InSAR results can be integrated as new geodetic constraints on the fault geometry and slip distribution [30,38–40]. Although the coseismic SRD map simply gives one-dimensional constraints on the coseismic displacement, it provides a much larger spatial coverage than the GPS network. To check the interest of such InSAR integration, we compare our results with two models of slip distribution, from Dominguez et al. [8] and Wang et al. [13]. These models are inverted with Okada's method in homogeneous elastic half-space [41,42]; we use the Range-Change programme [43] to reconstruct the predicted coseismic SRD. Although both these models are glob-

ally consistent in trend with our results, they tend to overestimate the displacements. For instance, regarding the model from Dominguez et al. [8], the rms difference between the model and the coseismic SRD map is 29 cm. Even excluding a 5 km wide strip along the fault trace, where the largest discrepancies may be expected (notably because of the approximate geometry of the fault used in the model), the rms difference remains as large as 15 cm. Moreover, it is noteworthy that the deformation pattern observed is smoother than those in the models. Model comparison with InSAR results is particularly interesting as it gives more precise information than comparison with GPS data on the spatial distribution of the model errors. In this way, we determined that the model of Dominguez et al. [8] significantly overestimates the coseismic SRD in the area between Pakuashan and the fault trace, which may result from approximations in modelling the local fault geometry. Concerning the regional overestimate of the coseismic displacement by the models, Ji et al. [14] noted that a layered-Earth model is better than the half-space model for generating static response. They indicated that for a thrust, the fault response generated by the half-space Earth model is, by 30% or more, larger than that obtained with the layered model in the footwall. Furthermore, because the largest coseismic displacements occur on the hangingwall, the inversions are certainly more influenced by the hangingwall data than by the footwall ones.

Considering a joint inversion including our results, the asymmetrical spatial distribution of InSAR measurement in the footwall only deserves consideration because it can introduce a bias on modelling [38]. Another problem, related to data uncertainty, is the weighting of the data from different sources, which may also introduce bias in the modelling [30].

Taking into account these precautions, our results provide new constraints to improve the present-day knowledge on the Chi-Chi earthquake through modelling, especially in terms of coseismic slip distribution or fault geometry. Our valuable records of coseismic displacement caused by the Chi-Chi earthquake are available in most of the footwall domain of the reactivated

Chelungpu fault. The use of InSAR combined with the GPS information enables us to produce a map of the coseismic displacement on the foot-wall with centimetre accuracy, and with high resolution especially in the Taichung area. This result allows us to detect the influence of the Changhua and Tuntzuchio faults on the coseismic displacement of the Chi-Chi earthquake, that we suppose to be caused by slight slip along these faults triggered by the Chi-Chi earthquake. Based on these observations, we also suppose the presence of another fault west of the Changhua fault where a similar anomaly of the coseismic displacement occurs. Thus, not only does the InSAR technique provide a powerful tool to extrapolate the results of geodetic analyses, but it also has high potential to reveal features that other methods fail to reveal because of their punctual character (GPS network or strong motion network) or limitation in accuracy (correlation of SPOT satellite images).

Acknowledgements

We thank J.-P. Avouac and S. Dominguez, who provided results in advance of publication, and also the GDR-INSAR group and the CSRSR Centre of the National Central University of Chungli (Taiwan) for their help. This work was supported by the European Space Agency (ESA EO project C1P-1046 and ESA AO project), by the Taiwan–France cooperation programme (French Institut in Taipei and National Science Council of Taiwan) and by the French CNRS-INSU in the framework of the PNRN. We are grateful to Hu Jyr-Ching and to the reviewers for their comments that improved the manuscript.
[AC]

References

- [1] H. Kao, W.P. Chen, The Chi-Chi earthquake sequence: Active, out-of-sequence thrust faulting in Taiwan, *Science* 288 (2000) 2346–2349.
- [2] T.C. Shin, T.I. Teng, An overview of the 1999 Chi-Chi, Taiwan earthquake, *Bull. Seismol. Soc. Am.* 91 (2001) 895–913.
- [3] T.L. Hsu, H.C. Chang, Quaternary faulting in Taiwan, *Mem. Geol. Soc. China* 3 (1979) 155–165.
- [4] A. Lin, T. Ouchi, A. Chen, T. Maruyama, Co-seismic displacements, folding and shortening structures along the Chelungpu surface rupture zone occurred during the 1999 Chi-Chi (Taiwan) earthquake, *Tectonophysics* 330 (2001) 225–244.
- [5] M. Yang, R.J. Rau, J.Y. Yu, T.T. Yu, Geodetically observed surface displacements of the 1999 Chi-Chi, Taiwan, earthquake, *Earth Planet. Space* 52 (2000) 403–413.
- [6] S.B. Yu, L.C. Kuo, Y.J. Hsu, H.H. Su, C.C. Liu, C.S. Hou, J.F. Lee, T.C. Lai, C.C. Liu, C.L. Liu, T.F. Tseng, C.S. Tsai, T.C. Shin, Preseismic deformation and coseismic displacements associated with the 1999 Chi-Chi, Taiwan, earthquake, *Bull. Seismol. Soc. Am.* 91 (2001) 995–1012.
- [7] C. Wu, M. Takeo, S. Ide, Source process of the Chi-Chi earthquake; a joint inversion of strong motion data and Global Positioning System data with a multifault model, *Bull. Seismol. Soc. Am.* 91 (2001) 1128–1143.
- [8] S. Dominguez, J.P. Avouac, R. Michel, Horizontal coseismic deformation of the 1999 Chi-Chi earthquake measured from SPOT satellite images: implications for the seismic cycle along the western foothills of Central Taiwan, *J. Geophys. Res.* 108,
- [9] Central Geological Survey, Map of the surface ruptures along Chelungpu fault during the Chi-Chi earthquake, Taiwan, scale 1:25,000, Central Geological Survey, Ministry of Economical Affairs, Taiwan, 1999.
- [10] Central Geological Survey, Report of the geological survey of the 1999 Chi-Chi earthquake (in Chinese), Central Geological Survey, Ministry of Economical Affairs, Taiwan, 1999, 315 pp.
- [11] K.F. Ma, J. Mori, S.J. Lee, S.B. Yu, Spatial and temporal distribution of slip for the 1999 Chi-Chi, Taiwan, earthquake, *Bull. Seismol. Soc. Am.* 91 (2001) 1069–1087.
- [12] K.M. Johnson, Y.J. Hsu, P. Segall, S.B. Yu, Fault geometry and slip distribution of the 1999 Chi-Chi, Taiwan earthquake imaged from inversion of GPS data, *Geophys. Res. Lett.* 28 (2001) 2285–2288.
- [13] W.H. Wang, S.H. Chang, C.H. Chen, Fault slip inverted from surface displacements during the 1999 Chi-Chi, Taiwan earthquake, *Bull. Seismol. Soc. Am.* 91 (2001) 1167–1181.
- [14] C. Ji, D.V. Helmberger, T.R.A. Song, K.F. Ma, D.J. Wald, Slip distribution and tectonic implication of the 1999 Chi-Chi, Taiwan, earthquake, *Geophys. Res. Lett.* 28 (2001) 4379–4382.
- [15] Centre National d'Etudes Spatiales (C.N.E.S.), PRISME/DIAPASON Software package, version 1.0, CNES, Toulouse, 1997.
- [16] D. Massonnet, F. Adragna, M. Rossi, CNES general-purpose SAR correlator, *IEEE Trans. Geosci. Remote Sens.* 32 (1994) 636–643.
- [17] D. Massonnet, K.L. Feigl, Radar interferometry and its application to changes in the Earth's surface, *Rev. Geophys.* 36 (1998) 441–500.

- [18] H.A. Zebker, J. Villasenor, Decorrelation in interferometric radar echoes, *IEEE Trans. Geosci. Remote Sens.* 30 (1992) 950–959.
- [19] H.A. Zebker, P.A. Rosen, S. Hensley, Atmospheric effects in interferometric synthetic aperture radar surface deformation and topographic maps, *J. Geophys. Res.* 102 (1997) 7547–7563.
- [20] F. Gatelli, M.A. Guarnieri, F. Parizzi, P. Pasquali, C. Prati, F. Rocca, The wavenumber shift in SAR interferometry, *IEEE Trans. Geosci. Remote Sens.* 32 (1994) 855–865.
- [21] R.F. Hanssen, *Radar Interferometry: Data Interpretation and Error Analysis*, Kluwer Academic, Dordrecht, 2001, 308 pp.
- [22] B. Fruneau, E. Pathier, D. Raymond, B. Deffontaines, C.T. Lee, H.T. Wang, J. Angelier, J.P. Rudant, C.P. Chang, Uplift of Tainan Tableland (SW Taiwan) revealed by SAR interferometry, *Geophys. Res. Lett.* 28 (2001) 3071–3074.
- [23] R. Scharroo, P. Visser, Precise orbit determination and gravity field improvement for the ERS satellites: Advances in oceanography and sea ice research: Using ERS observations, *J. Geophys. Res.* 103 (1998) 8113–8127.
- [24] GFZ/D-PAF GeoForschungsZentrum Potsdam, DLR precise orbits (ERS-1.ORB.PRC), ESA/ESRIN (1999).
- [25] F. Beauducel, P. Briole, J.L. Froger, Volcano-wide fringes in ERS synthetic aperture radar interferograms of Etna (1992–1998): Deformation or tropospheric effect?, *J. Geophys. Res.* 105 (2000) 16391–16402.
- [26] C.Y. Wang, L.H. Cheng, C.V. Chin, S.B. Yu, Coseismic hydrologic response of an alluvial fan to the 1999 Chi-Chi earthquake, Taiwan, *Geology* 29 (2001) 831–834.
- [27] R.M. Goldstein, H.A. Zebker, C.L. Werner, Satellite radar interferometry: two-dimensional phase unwrapping, *Radio Sci.* 23 (1988) 713–720.
- [28] R.M. Goldstein, C.L. Werner, Radar interferogram filtering for geophysical applications, *Geophys. Res. Lett.* 25 (1998) 4035–4038.
- [29] M. Murakami, M. Tobita, S. Fujiwara, T. Saito, H. Masaharu, Coseismic crustal deformations of 1994 Northridge, California, earthquake detected by interferometric JERS 1 synthetic aperture radar, *J. Geophys. Res.* 101 (1996) 8605–8614.
- [30] K.L. Feigl, F. Sarti, H. Vadon, S. McClusky, S. Ergintav, P. Durand, R. Burgmann, A. Rigo, D. Massonnet, R. Reilinger, Estimating slip distribution for the Izmit mainshock from coseismic GPS, ERS-1, RADARSAT, and SPOT measurements, *Bull. Seismol. Soc. Am.* 92 (2002) 138–160.
- [31] J.F. Genrich, Y. Bock, R.G. Mason, Crustal deformation across the Imperial Fault: results from kinematic GPS surveys and trilateration of a densely spaced, small-aperture network, *J. Geophys. Res.* 102 (1997) 4985–5004.
- [32] T.J. Wright, Remote monitoring of the earthquake cycle using satellite radar interferometry, *Philos. Trans. R. Soc. Lond. A* 360 (2002) 2873–2888.
- [33] M.G. Bonilla, A review of recently active faults in Taiwan, U.S. Geological Survey Open-File Report, 1975, 58 pp.
- [34] N. Bechor, P. Segall, J. McGuire, Y.J. Hsu, S.B. Yu, Post-seismic slip following the 1999 Chi-Chi Taiwan earthquake, in: 2001 Joint Geosciences Assembly, Proc. Int. Symposium on Earthquake and Active Tectonics, Taipei, 2001, p. 15.
- [35] Y.J. Hsu, S.B. Yu, L.C. Kuo, H.Y. Chen, K.F. Ma, Post-seismic deformation following the 1999 Chi-Chi, Taiwan earthquake, in: 2001 Joint Geosciences Assembly, Proc. Int. Symposium on Earthquake and Active Tectonics, Taipei, 2001, p. 12.
- [36] Y. Zeng, C.H. Chen, Fault rupture process of the 20 September 1999 Chi-Chi, Taiwan, earthquake, *Bull. Seismol. Soc. Am.* 91 (2001) 1088–1098.
- [37] W.C. Chi, D. Dreger, A. Kaverina, Finite-source modeling of the 1999 Taiwan (Chi-Chi) earthquake derived from a dense strong-motion network, *Bull. Seismol. Soc. Am.* 91 (2001) 1144–1157.
- [38] B. Delouis, D. Giardini, P.R. Lundgren, J. Salichon, Joint inversion of InSAR, GPS, teleseismic, and strong-motion data for the spatial and temporal distribution of earthquake slip: Application to the 1999 Izmit mainshock, *Bull. Seismol. Soc. Am.* 92 (2002) 278–299.
- [39] T.J. Wright, B.E. Parsons, J.A. Jackson, M. Haynes, E.J. Fielding, P.C. England, P.J. Clarke, Source parameters of the 1 October 1995 Dinar (Turkey) earthquake from SAR interferometry and seismic bodywave modelling, *Earth Planet. Sci. Lett.* 172 (1999) 23–37.
- [40] R. Burgmann, M.E. Ayhan, E.J. Fielding, T.J. Wright, S. McClusky, B. Aktug, C. Demir, O. Lenk, A. Turkezer, Deformation during the 12 November 1999 Düzce, Turkey, earthquake, from GPS and InSAR data, *Bull. Seismol. Soc. Am.* 92 (2002) 161–171.
- [41] Y. Okada, Surface deformation due to shear and tensile faults in a half-space, *Bull. Seismol. Soc. Am.* 75 (1985) 1135–1154.
- [42] Y. Okada, Internal deformation due to shear and tensile faults in a half-space, *Bull. Seismol. Soc. Am.* 82 (1992) 1018–1040.
- [43] K.L. Feigl, E. Dupre, RINGCHN: a program to calculate displacement components from dislocations in an elastic half-space with applications for modeling geodetic measurements of crustal deformation, *Comput. Geosci.* 25 (1999) 695–704.
- [44] Y. Fialko, D. Sandwell, D.C. Agnew, M. Simons, P. Shearer, B. Minster, Deformation on nearby faults induced by the 1999 Hector Mine earthquake, *Science* 297 (2002) 1858–1862.